Post-Print

Numerical Characterization of the Vortex Flow and Aerodynamic Performance of a Reverse Delta Wing

Ahmed Osama Mahgoub* and Luca Cortelezzi[†]
Department of Aerospace Science and Technology
Polytechnic University of Milan, 20156, Milan, Italy

We simulate numerically the unsteady flow past a reverse delta wing to characterize the structure of the vortical flow and associated unsteady phenomena, and quantify the impact of such structures on the aerodynamic performance. We select the most cost-effective grid-size/time-step combination by performing a coupled sensitivity analysis. We successfully validate our numerical approach against well established results for a delta wing. We establish that the flow past a reverse delta wing is always unsteady even at small angles of attack. The shear layer separating at the leading edge of the reverse delta wing rolls-up into spanwise vortical structures that, as they are convected downstream, pair, realign and reorganize generating suction that contributes substantially to the lift produced by a reverse delta wing. The tip vortices confine the vortical structures to the leeward side and contribute to a less extent to lift. Power spectral density analysis shows that the unsteadiness of the lift coefficient is related to vortex shedding and reorganization of the vortical structures. Finally, we confirm that the lift-to-drag ratio of a delta wing and a reverse delta wing is, surprisingly, about the same.

Nomenclature

a_∞	=	Free stream speed of sound (m/s)
c	=	Wing mid chord (m)
C_D	=	Drag coefficient
C_L	=	Lift coefficient
C_m	=	Pitching moment coefficient
C_p	=	Pressure coefficient
D	=	Drag force (N)
f	=	Frequency (1/s)
k	=	Turbulent kinetic energy (m^2/s^2)

---

*Master's student, Department of Aerospace Science and Technology, Via Giuseppe La Masa, 34, 20156, Milan, Italy; ahmedosama.mahgoub@mail.polimi.it. Current Address: Qatar University, Doha, Qatar

[†]Associate Professor, Department of Aerospace Science and Technology, Via Giuseppe La Masa, 34, 20156, Milan, Italy; luca.cortelezzi@polimi.it.

L	=	Lift force (N)
$M_{c/4}$	=	Pitching moment (N.m)
M_∞	=	Free stream Mach number
p	=	Non-dimensional pressure
$p^\star$	=	Dimensional pressure (Pa)
q_∞	=	Free stream dynamic pressure (Pa)
Re_∞	=	Free stream Reynolds number
S	=	Reference area (m^2)
St	=	Strouhal number
t	=	Non-dimensional time
$t^\star$	=	Time (s)
t	=	Non-dimensional time
Δt	=	Non-dimensional time step
$\Delta t^\star$	=	Time step (s)
$\mathbf{u}$	=	Non-dimensional velocity vector
u, v, w	=	Non-dimensional x, y and z velocity components
U_∞	=	Free stream velocity (m/s)
x, y, z	=	Cartesian coordinates (m)
y^+	=	Normalized wall distance
α	=	Angle of attack (deg)
ε	=	Dissipation rate of turbulent kinetic energy (m^2/s^3)
ν	=	Kinematic viscosity (Pa $\cdot$ s)
ω	=	Specific dissipation rate (1/s)
ρ	=	Density (kg/m^3)
ζ_y	=	Non-dimensional y-component of the vorticity field

I. Introduction

Delta wings (DWs) have been and are used extensively and successfully, mostly in military high-speed applications, because of their aerodynamic superiority with respect to conventional wings. DWs owe their superiority to two large vortices generated by the roll-up of the shear layers separating from the leading edges of a DW. These leading edge vortices, lying on top of the DW, induce a substantial amount of suction on the leeward side that contributes significantly to the lift generated by a DW. Differently from DWs, reverse delta wings (RDWs) have been used only in a

few near-ground low-speed applications. In the case of a RDW the structure of the vortical flow around the RDW and its contribution to the generation of lift is not completely understood. Such flow has been sparsely studied experimentally and even less numerically. This article intends to shed light on the formation and time evolution of the vortical flow past a RDW and characterize the impact of the vortical flow on the aerodynamic performance of a RDW.

Early applications of RDWs are due to Lippisch (1965 and 1969) [1, 2]. He conceived seaplanes designed to fly close to sea-level, also known as wing-in-ground-craft (WIG-craft), by leveraging the stabilizing pitching moment induced by RDW in ground effect. A totally different application was patented by Gerhardt (1996) [3], who designed a supersonic natural laminar flow RDW. Gerhardt noted that when a DW and a RDW fly at supersonic speed, they experience about the same values of wave drag and skin-friction drag. However, due to a more favorable pressure gradient over the RDW, a laminar flow covering almost 50% of the RDW area can be achieved, generating a substantial drag reduction.

Recently, Urquhart *et al.* (2006) [4] studied experimentally the performance of a Lippisch WIG-craft. They showed that the lift-to-drag ratio increases substantially when the ground clearance decreases, up to twice the value in free-stream flight. Altaf *et al.* (2011) [5] experimentally investigated the aerodynamics of a DW and a RDW at the same flow conditions. They reported that a RDW has lower lift and drag coefficients values than a DW, but it has a higher lift-to-drag ratio. Furthermore, they concluded that a RDW has a lower adverse pressure gradient along the chord than a DW. More recently, Lee and co-workers [6–8] also studied experimentally the aerodynamics of a DW and a RDW at the same flow conditions. They showed that a RDW has a larger stall angle than a DW. On the other hand, they assessed, contrary to the findings of [5], that a RDW has a lower lift-to-drag ratio than a DW.

Figure 1 shows two visualizations of the flowfield past a RDW at an angle of attack of 20°. Panel (a) presents the top view of a smoke visualization at $Re_\infty \approx 10^4$ (Ko, 2016 [7]), while panel (b) presents the side view of a dye visualization at $Re_\infty = 2.70 \times 10^5$ (Mou, 2015 [6]). Although, the visualizations have been performed at substantially different Reynolds numbers, they provide great insight into the complexity of the vortical structures present in the flow past a RDW. Two are the main features of the vortical flow: the tip vortices and the spanwise vortex filaments (SVF's). Recently, Lee and He (2018) [9] showed that the tip vortices (see figure 1 (a)) partially contribute to the lift produced by a RDW. Figure 1 (b) shows that the spanwise vortical structures are generated by the roll-up of the shear layer separating from the leading edge of the RDW. Ko concluded that most of the lift produced by a RDW is due to the spanwise vortices and that the stall of a RDW is strongly related to the destruction of the spanwise vortex filaments. This article investigates extensively the generation, convection and reorganization of the vortical structures present over the leeward side of a RDW.

A few studies investigated means to enhance the aerodynamic performance of RDWs. Lee (2016) [10] showed that the effect of gurney flaplike strips assembled to the sides of a RDW is to produce a larger increase in lift than in drag, resulting in a better lift-to-drag ratio. Different are the effects of a gurney flap assembled to the leading edge. On the one hand, an upward gurney flap induces more diffused wing tip vortices and a reduction of the lift coefficient
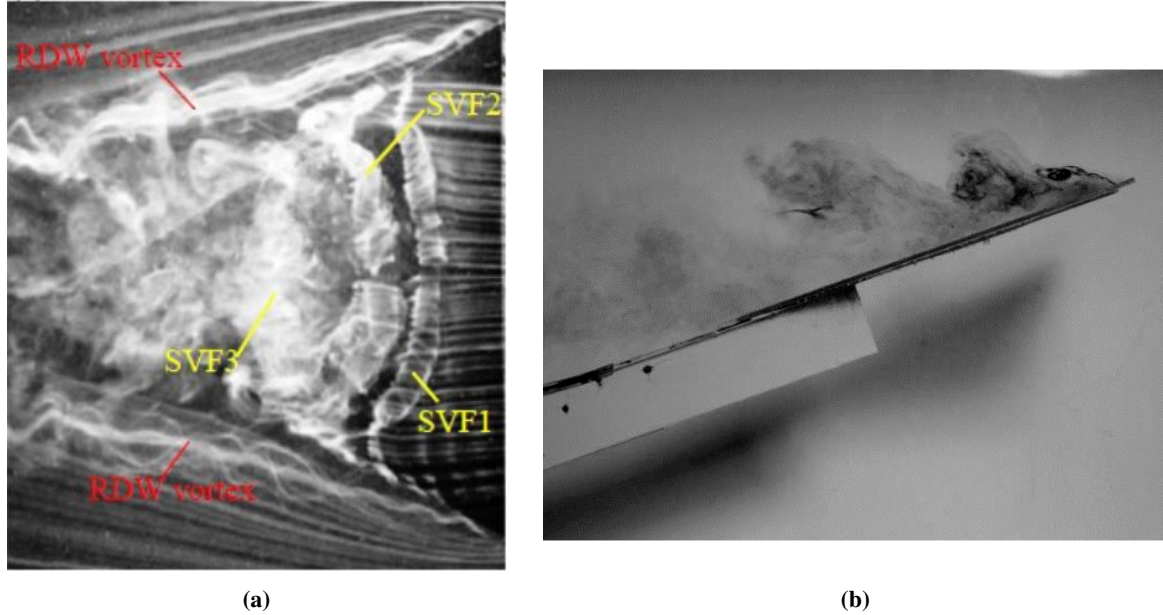
Fig. 1 **Flow visualizations of the vortical structures over the leeward side of a RDW at an angle of attack of** $20°$**. Panel (a): Top view of a smoke visualization [7] at** $Re_\infty \approx 10^4$**. Panel (b): Side view of a die visualization [6] at** $Re_\infty = 2.70 \times 10^5$**. Images reproduced with permission.**

values in pre-stall flight conditions. On the other hand, a downward gurney flap increases the maximum value of the lift coefficient. Lee [11] also investigated the effect of anhedral on a RDW and showed that anhedral decreases the lift coefficient and, therefore, the lift-to-drag ratio of a RDW.

Attempts have been made to modify the geometry of the planform in order to improve the aerodynamic performance of a RDW. Lee and He (2018) [9] reported that the back apex region of a RDW contributes negligibly to lift production but, on the other hand, at high angles of attack it triggers the destruction of the spanwise vortex filaments leading to stalling. Therefore, they tested a 30% cropped RDW, noticing minor changes in the aerodynamic properties (with respect to the baseline RDW) accompanied by a beneficial weight reduction. Finally, they showed that the lift of a cropped RDW was significantly enhanced by mounting Gurney flaplike side-edge strips. Lee [11] also investigated the effect of anhedral on a RDW and showed that anhedral has the negative effect to decrease the lift coefficient.

RDWs have also found applications in passive flow control [12–14]. Lee and Su (2012) [12] studied experimentally the aerodynamic performance of a conventional wing with a deflectable half RDW mounted at its tip, as a means to control passively the wing tip vortex. They reported that, regardless of the angle of deflection, the induced drag of the modified wing is always lower than the baseline wing. Alternatively, Altaf *et al.* used a full RDW mounted at the end of a wing [14] or a flap [13] for tip vortex alleviation. They found that in both cases the RDW addon weakens the tip vortex by reducing its tangential velocity, maximum core vorticity and its circulation.

To the best of our knowledge, the only numerical simulations of the flow past a RDW available in literature have been performed by the same research group [5, 16]. Since, the numerical results appear to be identical, we will discuss
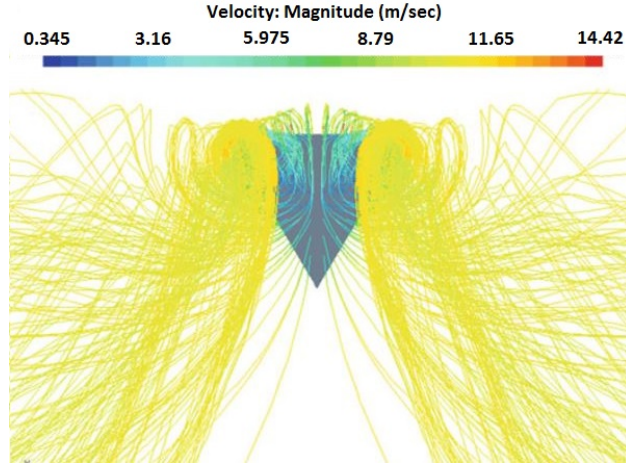
Fig. 2 **Streamlines, colored by the local velocity magnitude values, of a flow past a RDW at an angle of attack** $\alpha = 25°$ **generated by a steady state numerical simulation [16]. Image reproduced with permission.**

them together. The authors performed steady state numerical simulations of the flow past a DW and a RDW at angles of attack $\alpha = 25°$, $30°$ and $40°$, using as turbulence model a RANS kε-model and imposing symmetry along the chords of the wings [17]. Figure 2 shows the steady state flow field estimated numerically. The comparison with figure 1 clearly shows the pitfalls of simulating an unsteady flow with a steady state simulation. As we will show in our study, the flow past a RDW is always unsteady, at any angle of attack, and, therefore, it is essential to perform unsteady simulations for reproducing accurately the flow past a RDW.

In this study, we simulate numerically the flow past a DW and a RDW at $Re_\infty = 3.4 \times 10^5$ for the range of angles of attack $0° \leq \alpha \leq 20°$. We limit the maximum angle of attack to $\alpha = 20°$, to be sure that the flow past the DW and RDW is unstalled. The geometry of the wing planform is the same for both DW and RDW, and replicates exactly the geometry of the $65°$ sweep angle planform used by Lee and co-workers in their experimental studies [6–8, 10]. The results of these studies will be used, among others, to validate and corroborate our results.

We perform our unsteady numerical simulations using the commercial software ANSYS Fluent 17.2, which is based on a finite-volume method. As a turbulence model, we use Delayed Detached-Eddy Simulation (DDES) [18] in conjunction with the kω Shear Stress Transport (SST) [19, 20] (with curvature correction) as a Reynolds-Averaged Navier-Stokes (RANS) model. We perform a combined grid-size/time-step sensitivity study following Cummings *et al.* (2008) [15], who analyzed the effects of time step, grid sizing and turbulence models on the accuracy of unsteady flow simulations, providing a useful framework for selecting a cost-effective grid-size/time-step combination. We use the flow past a DW, a very well known and studied flow, to design, test and validate, against several experimental studies, our numerical simulations. Following the successful validation, we perform unsteady numerical simulations of flows past a RDW using the same grid (turned by $180°$) and time step used for a DW.

This article presents results from accurate unsteady numerical simulations of flows past RDWs. We will analyze in

details the formation and evolution of the vortical structures that characterize the flow past a RDW. A power spectral density analysis allows us to identify the dominant sources of unsteadiness, mainly the reorganization of the vortical structure generated by the roll-up of the shear layer separating from the leading edge of the RDW. We will show that these vortical structures are responsible for inducing a substantial amount of suction on the leeward side of the RDW contributing substantially, although unsteadily, to the total lift produced by a RDW.

This article is organized as follows: Section 2 presents the mathematical model and the methodology used to perform accurate numerical simulations. Section 3 presents a coupled sensitivity study leading to the selection of a cost-effective grid-size/time-step combination. Section 4 presents our flow visualizations, power spectral density analyses, and estimates of the aerodynamic coefficients. Finally, in Section 5, we present the concluding remarks.

II. Mathematical model and numerical solution

In this study we simulate flows past DWs and RDWs at velocities low enough to neglect the effect of compressibility, i.e., flows at Mach numbers $M_\infty = U_\infty/a_\infty < 0.1$, where U_∞ is the free stream velocity and a_∞ is the speed of sound in air. The equations that govern the motion of an incompressible viscous fluid past a DW or a RDW are continuity and momentum equations. We make the problem dimensionless by defining as a characteristic length the wing mid-chord c and as a characteristic time U_∞/c. The dimensionless equations are:

$$
\begin{aligned}
\nabla \cdot \mathbf{u} &= 0, \\
\frac{\partial \mathbf{u}}{\partial t} + (\mathbf{u} \cdot \nabla)\mathbf{u} &= \frac{1}{Re_\infty}\nabla^2\mathbf{u} - \nabla p,
\end{aligned}
\tag{1}
$$

where $\mathbf{u} = [u, v, w]^T$ is the velocity vector field, p is the pressure field and Re_∞ is the free stream Reynolds number, which is defined as $Re_\infty = U_\infty c/\nu$, where ν is the kinematic viscosity of the fluid. Note that from here on all mathematical symbols will represent dimensionless quantities, unless otherwise specified.

We solve numerically the above equations using the commercial software ANSYS Fluent 17.2, which is based on a finite-volume method. As a turbulence model we use Delayed Detached-Eddy Simulation (DDES) [18] in conjunction with the kω Shear Stress Transport (SST) [19, 20] (with curvature correction) as a Reynolds-Averaged Navier-Stokes (RANS) model. To set the turbulence model up, we use the default options implemented in ANSYS Fluent 17.2. Since compressibility effects are negligible, we choose a pressure based solver and a coupled algorithm for the pressure-velocity coupling. In details, the solver performs the gradients evaluation using a least-squares cell based method and the pressure interpolation using a second-order scheme. A second-order upwind scheme is used for the convective terms of the momentum, turbulent kinetic energy (k) and specific dissipation rate (ω) equations. Time integration is performed using a bounded second-order implicit scheme. Numerical simulations have been performed using 50 logical cores of a computer equipped with a processor Intel® Xeon Phi™ 1.30GHz, with 64 physical cores and four threads for each core,

6

and 112 GB of RAM.

III. Grid-size/time-step sensitivity study

To choose the most cost-effective grid-size/time-step combination for our simulations, we implemented the method proposed by Cummings *et al.* [15], which consists in constructing three grids of different sizes (coarse, medium and fine) and selecting six different time steps, one double of the other. The two smallest time steps are used with the fine grid, the two middle time steps with the medium grid, and the two largest time steps with the coarser grid, which results in six grid-size/time-step pairs. To select the most cost-effective gird-size/time-step combination, we performed six simulations, using each pair of grid-sizes/time-steps, of a flow past a DW at angle of attack $\alpha = 20°$ and $Re_\infty = 3.4 \times 10^5$. We selected such a flow because, under these conditions, the leading edge vortices undergo to a helical breakdown, which induces unsteady aerodynamic forces characterized by oscillations having well defined, primary and secondary, frequencies. For each simulation, we performed a power spectral density analysis of the time histories of the unsteady aerodynamic forces to detect the variations of the primary and secondary frequencies associated with vortex breakdown and other unsteady phenomena. The most cost-effective grid-size/time-step combination is the one for which the primary and secondary frequencies do not change appreciably when further reducing the time step or a using a finer grid.

A. Grid generation

The geometry of the wing planform (for the DW or RDW) chosen in this study is exactly the same as the one used by Lee and co-workers [6–8, 10], because we want to compare our numerical results with their experimental findings. The slender DW (or RDW) has a chord of $c = 0.42m$, a sweep angle of $65°$ and a thickness of $0.63cm$. Its three sides are beveled at $15°$. As it will be discussed later, to reduce the computational cost, we impose symmetry with respect to the middle-plane of the planform.

The computational domain for the symmetric case is 41 chords long, 10.5 chords wide and 20 chords high, see figure 3. The size of the fluid domain is sufficiently large to simulate far-field conditions, and we verified that the results of the simulations are independent of the size of the domain.

In order to perform a grid sensitivity study, we generated around half of the wing planform three grids of different resolutions: coarse, medium and fine (see figure 3). All grids comprise of a structured grid wrapped around the half-wing and an unstructured grid that fills the remaining of the computational domain, see figure 3. Note that the structured grid, designed to resolve accurately the flow within the boundary layer region, is the same for all cases, while the density of the unstructured grid changes from case to case. These grids are conceived to be used for both the DW and RDW by simply rotating the grid by $180°$, mimicking the experimental setup used by Lee and co-workers where the wing planform is mounted in the wind tunnel straight or rotated by $180°$ [6–8, 10].

To generate a structured grid, we created a subdomain wrapped around the planform (see figure 3(b)), whose

thickness is about equal to the thickness of the turbulent boundary layer that develops over a flat plate at the same Reynolds number. Following Cummings *et al.* [15] guidelines for correctly resolving a turbulent boundary layer, we selected the combined thickness of the first two cells next to the wall to be always less than $y^+ = 5$, i.e., we always have two cells within the viscous sub-layer. Recall, that in spatially developing turbulent boundary layer, the value of the wall units changes along the boundary layer. Furthermore, we set to 20 the number of cells in the normal direction to the wall. As a result, we obtained a structured grid where the thickness of the first cell next to the wall corresponds to maximum value of $y^+ = 2$, and an average value of $y^+ = 1$, while the thickness growth rate of the 20 cells is 1.2. The grid cells used within the boundary layer subdomain are either prisms or hexahedrals.

We used ANSYS meshing software with different relevance centers to generate automatically unstructured grids of different densities to fill the domain outside the boundary layer region. In this case, the grid cells are tetrahedrals. Table 1 reports the geometric and quality parameters for each of the three grids. Poor quality cells are those who have high skewness (close to 1), or an aspect ratio much larger than one. In all three grids, the number of poor quality cells is negligible compared to the total number of cells. Furthermore, the values reported in Table 1 are within the limits suggested by ANSYS Fluent and, therefore, acceptable.

Figure 3 (a) shows the fine grid for the full computational domain, where the inlets, outlets and symmetry plane are identified. Figure 3 (b) shows the grid generated at the wing surface and at the symmetry plane.

Table 1   Geometrical and quality parameters of the three grids considered: first column coarse grid, middle column medium grid and last column fine grid. CPU run time for each grid-size/time-step pair: last two rows

		Coarse		Medium		Fine	
Mesh size	**Relevance center**	Medium		Fine		Fine	
	Growth rate	1.2		1.2		1.07	
	Number of cells	3465493		6143440		8653808	
Quality	**Maximum aspect ratio**	252.09		265.02		237.56	
	Maximum skewness	0.978		0.975		0.975	
	Minimum orthogonal quality	2.21e-2		3.46e-2		3.46e-2	
CPU time	**Non-dimensional time step (Δt)**	0.32	0.16	0.08	0.04	0.02	0.01
	Total run time (days)	≈ 1.5	≈ 3	≈ 5	≈ 10	≈ 20	≈ 40

B. Sensitivity analysis

A correct grid-size/time-step selection is essential for simulating accurately and efficiently unsteady flows that include regions of separated flows with vorticity fluctuations. As a rule of thumb for performing accurate unsteady simulations, Cummings *et al.* [15] suggest to use as a non-dimensional time step $\Delta t = (\Delta t^\star / U_\infty)c \leq 0.01$, where $\Delta t^\star$ is the dimensional time step in seconds. To perform our sensitivity study, we select six non-dimensional time steps $\Delta t = 0.01, 0.02, 0.04, 0.08, 0.16$ and 0.32 to be used in conjunction with the three grids described above. The two smaller
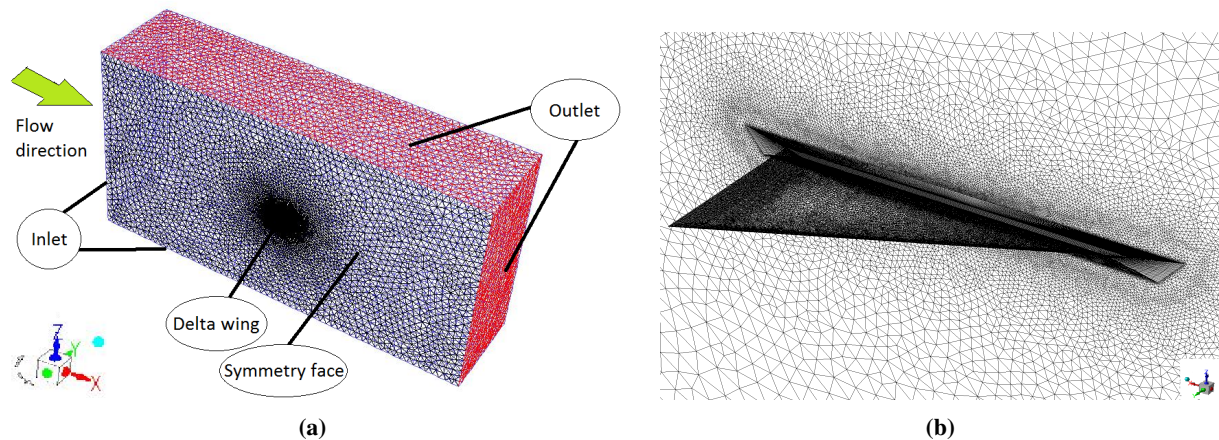
Fig. 3 Isometric view of the fine grid domain for the half wing planform: (a) whole fluid domain and (b) grid at the wing planform and at the symmetry plane, rotated by $180°$ with respect to panel (a).

time steps are used with the finer grid, the two medium time steps with the medium grid and the two larger time steps with the coarse grid.

Note that within each time step, we used five internal sub-iterations only because, as suggested by Cummings *et al.* [15], there is no improvement in convergence when using a higher number of sub-iterations. In the last two rows of table 1 we report the total run time required to complete a simulation using each grid-size/time-step pair. As it can be seen, the numerical simulations are computationally very expensive, and therefore, justify our choice for imposing symmetry at the middle plane.

To select the most cost-effective grid-size/time-step combination, we perform six simulations, one for each grid-size/time-step combination, of the flow past a DW at an angle of attack $\alpha = 20°$ and Reynolds number $Re_\infty = 3.4 \times 10^5$. Under these conditions the flow over the DW is unsteady, because the leading edge vortices undergo to vortex breakdown near the trailing edge modifying the mechanism of vortex shedding. These unsteady phenomena are characterized by well-defined frequencies of oscillations that affect the aerodynamic forces [21]. To identify these frequencies, we compute the power spectral density (PSD) of the time history of the lift coefficient, C_L, after removing the initial transient. The lift and drag coefficients, C_L and C_D, are defined as $C_L = L/(q_\infty S)$ and $C_D = D/(q_\infty S)$, where L and D are the total lift and drag forces, q_∞ is the dynamic pressure at the free stream, defined as $q_\infty = 0.5\rho_\infty U_\infty^2$, and S is the reference area.

Figure 4 presents the instantaneous iso-surface, at time $t = 176.6$, of vorticity magnitude 35.5, colored in proportion to the values of the pressure coefficient C_p, visualizing part of the separated shear layer (in dark gray/black) and the cores of the primary vortices (in light gray), of a DW at angle of attack $\alpha = 20°$ and $Re_\infty = 3.4 \times 10^5$. The pressure coefficient C_p is defined as $C_p = (p^\star - p^\star_\infty)/q_\infty$, where $p^\star$ and $p^\star_\infty$ are the pressure values at the corresponding point

and at free stream. Figure 4 shows that the cores of the primary vortices undergo to a spiral vortex breakdown (in gray) near the trailing edge. This result shows the FLUENT is able to predict the vortex breakdown and its location, reproducing the diffused vortex core and spiral vortex motion [23, 24], contrary to what is reported by Robertson *et al.* [22]. Figure 4 shows also that the vorticity produced by the separating shear layer over the leeward side of the DW leaves the trailing edge and creates a wake. However, the details of the vortical structures in the wake of the DW are not captured beyond half a chord past the trailing edge, because the vorticity magnitude is too small and the grid, for computational efficiency, is less refined in the far field.
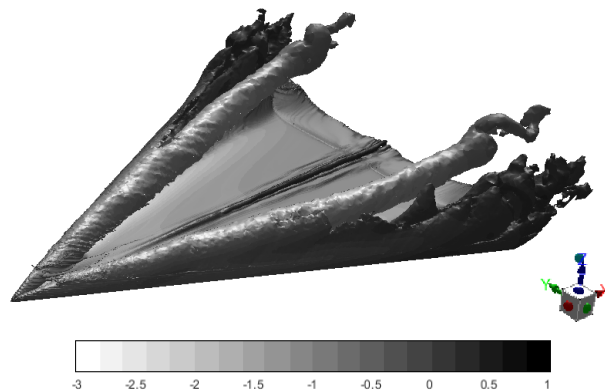

Fig. 4 **Instantaneous iso-surface, at time** $t = 176.6$**, of vorticity magnitude 35.5, colored in proportion to the values of the pressure coefficient** C_p**, visualizing the spiral breakdown of the cores of the primary vortices over a DW at angle of attack** $\alpha = 20°$ **and** $Re_\infty = 3.4 \times 10^5$**.**

The plot in figure 5 summarizes the results of our combined grid-size/time-step sensitivity study. It shows wave numbers, i.e. the inverse of the Strouhal numbers, $St^{-1} = (fc/U_\infty)^{-1}$, corresponding to the primary (black solid circles) and secondary (gray solid squares) frequencies, versus time steps, Δt. Note that we plot wave numbers versus time steps instead of frequencies versus time steps, because the former approach generates a plot the clearly visualizes the convergence of the sensitivity study. Figure 5 shows that the pairs of wave numbers decrease substantially as the coarseness of the grid and the size of the time step decrease. In the case of the fine grid, the two smaller time steps produce nearly the same wave numbers and. therefore, we consider the sensitivity study converged. Consequently, we conclude that the combination of the fine grid with the time step $\Delta t = 0.02$ is the most cost-effective combination for performing accurate simulations of unsteady flows over a DW/RDW. Note that the identified primary frequency corresponds to a Strouhal number of about 0.25, while the secondary frequency to a Strouhal number of about 0.4 which, according to Menke *et al.* [21] (1999), are both associated to the vortex shedding at a trailing edge of the DW.
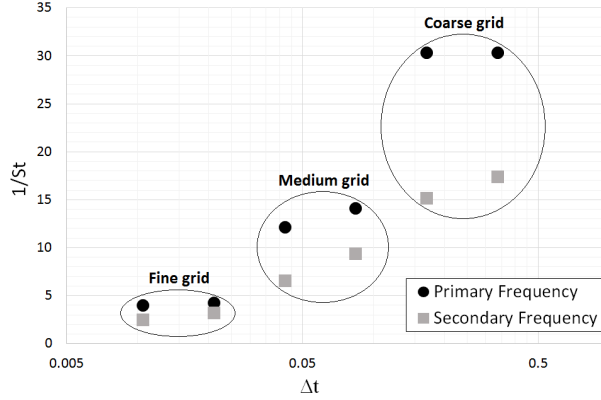
Fig. 5 **Wave numbers corresponding to the estimated primary (black solid circles) and secondary (gray solid squares) frequencies as a function of grid size and time step.**

IV. Results

Based on the results of our sensitivity study, we performed simulations of flows past DW and RDW at $Re_\infty = 3.4 \times 10^5$ using the fine grid and time step $\Delta t = 0.02$. In this section we present the results of our simulations in the form of flow visualizations, power spectral density (PSD) analysis of unsteady phenomena and characterization of aerodynamic forces.

A. Flow visualizations

Figure 6 shows the instantaneous iso-surfaces of vorticity magnitude 10.65 (panel (a)) and 24.85 (panel (b)), over the leeward side of a RDW at angles of attack $\alpha = 10°$ (panel (a)) and $20°$ (panel (b)) colored in proportion to the values of the pressure coefficient C_p at time $t = 150.52$ and $Re_\infty = 3.4 \times 10^5$. In both cases, the structures of the vortical flows appear to be similar. Two are the main features: (1) the roll-up of the shear layer, separating from the leading edge, that produces the spanwise vortical structures and (2) the tip vortices, that form at the ends of the leading edge. Further insight on the structure of the vorticity field is obtained by comparing figures 6 (b) and 1 (a). Note that a direct comparison cannot be made because the Reynolds number of the smoke visualization is substantially lower than ours, i.e. $Re \sim 10^4$. Also, the different view angles and means of visualization preclude a precise comparison. Nevertheless, these figures complement each other and permit a good assessment of the structure of the vorticity field.

In both panels of figure 6, the separating shear layer is visualized by the smooth part of the iso-surface that departs from the leading edge. In both cases, the shear layer rolls up forming spanwise vortical structures that pair with each other and reorganize themselves as they are convected downstream, creating a complex narrow wake confined by the tip vortices. The spanwise vortical structures are responsible for a substantial portion of the lift generated by a RDW, and they correspond to the structures visualized in figure 1 (a). The intensity of these vortical structures and the magnitude of the pressure field that they induce can be inferred by the color of the iso-surfaces: light gray/gray/dark gray at $\alpha = 10°$
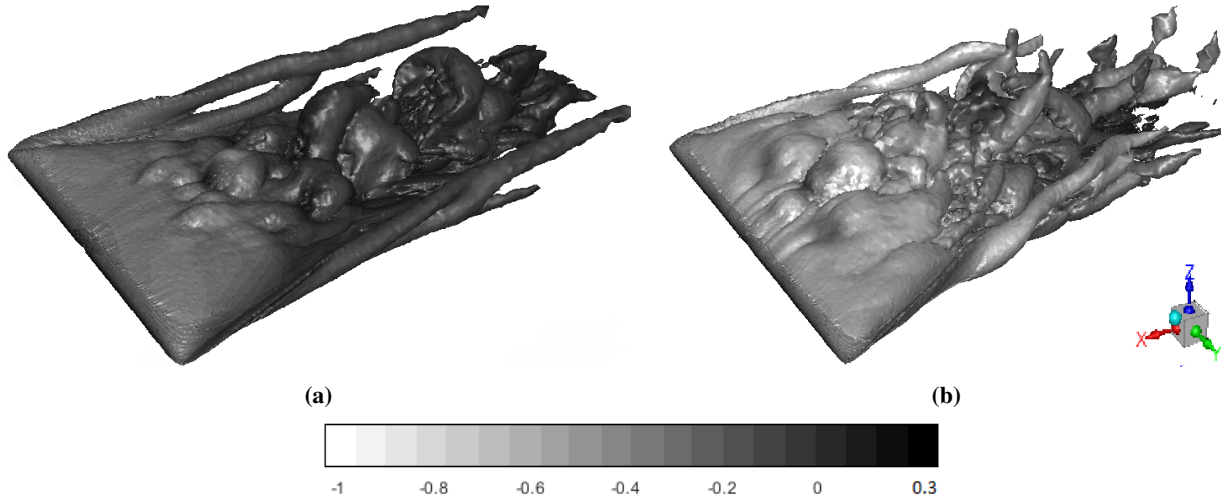
11

Fig. 6 **Instantaneous iso-surfaces of vorticity magnitude (10.65 (a) and 28.4 (b)) over the leeward side of a RDW at angles of attack $\alpha = 10°$ (a) and $20°$ (b) colored in proportion to the values of the pressure coefficient C_p, at time $t = 150.52$ and $Re_\infty = 3.4 \times 10^5$**

(panel (a)) and white/light gray/gray at $\alpha = 20°$ panel (b)). The sequence of colors and the shape of the vorticity iso-surfaces show that the vortical structures pair, realign and weaken as they are convected downstream implying the existence of an unsteady pressure distribution on the leeward side of the RDW.

The mechanism behind the formation of the tip vortices and their contribution to lift is not completely understood. We present the following argument that, in our opinion, fits experimental and numerical observations. To gain insight, we discuss and compare flows over rectangular, delta and reverse-delta wings. For simplicity, we assume that all planforms are perfectly flat, rigid and of negligible thickness, and posed at a positive angle of attack. First of all, since all the wings are assumed at a positive angle of attack, the pressure on the windward side of all planforms is higher than the ambient pressure and the pressure on the leeward side. As a consequence of the pressure differential, fluid tends to escape the windward side forcing the flow to separate at the edges of the planforms forming shear layers (or, conceptually, a vortex sheets) that, for their nature, tend to roll-up. In the case of a rectangular wing, the flow separates at the tip of the wing from its windward side, the shear layer rolls up over the back part of the tip of the wing forming a tip vortex. In the case of a DW, the flow also separates from the windward side but the shear layer rolls up over the leeward side because the span of the DW increases continuously moving down stream. In other words, the clever DW design force the shear layers to roll up over the leeward sides forming the so-called leading-edge vortices that are responsible for a substantial enhancement of the lift produced by a DW.

In the case of a RDW the flow also escapes the high pressure windward side separating, both, at the leading edge and at the side edges. The former separation contributes to the formation of the spanwise vortical structures, while the latter to the generation of the tip vortices. The shear layer separating from the side-edge rolls up away from the wing planform because the span of a RDW decreases continuously moving down stream. This mechanism is clearly
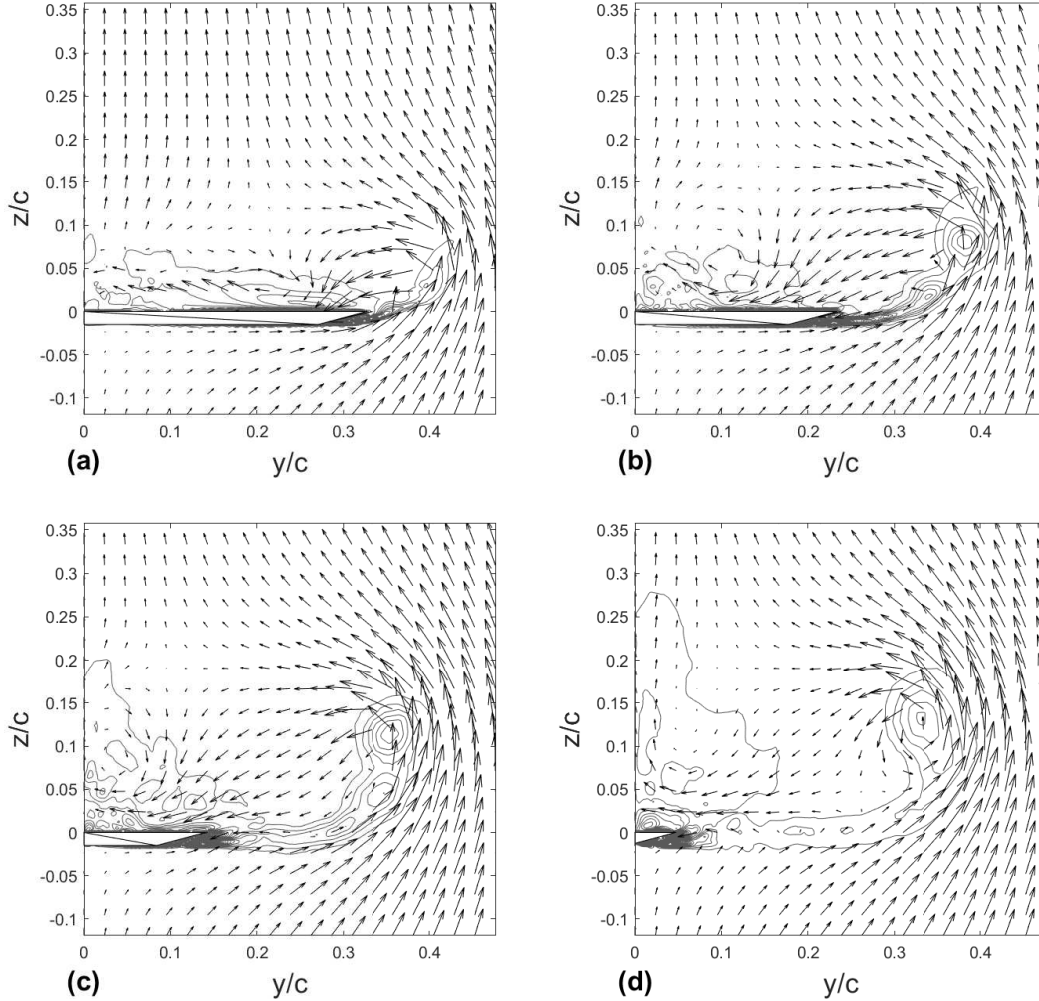
Fig. 7 **Averaged cross-sectional velocity vetor field superimposed to the contours of** x-**component of vorticity for a RDW at of** $\alpha = 10°$ **and** $Re_\infty = 3.4 \times 10^5$ **at chordwise stations x/c = 0.3 (a), 0.5 (b), 0.7 (c) and 0.9 (d).**

visualized in figure 7, which shows the averaged cross-sectional velocity vector field superimposed to the contours of x-component of the vorticity field at various chordwise stations, for a RDW at $\alpha = 10°$ and $Re_\infty = 3.4 \times 10^5$. The vorticity countors show the shear layer separating from the windard side nearly parallel to the planform. Apparently, it is as if the shear layer replaces the receding planform, creating a barrier between the flows on the windward and leeward sides. The velocity vector field shows that the downwash induced by the tip vortex impacts on a limited area of the wing along the side edge, an effect that decreases along the planform. Furthermore, the velocity vector field seems to indicate that the flow induced by the tip vortex is entrained by the spanwise vortices. The latter vortices are generated by the roll up of the shear layer separating at the leading edge. Figure 1 shows a top view on panel (a) ($Re_\infty \sim 10^4$) and a cross sectional view in panel (b) ($Re_\infty = 2.7 \times 10^5$) of the spanwise vortices.

Apparently, the formation and evolution of the tip vortices and spanwise vortices is independent of each others. Nevertheless, the tip vortices, which contribute little to the production of lift, seem to have a beneficial effect by
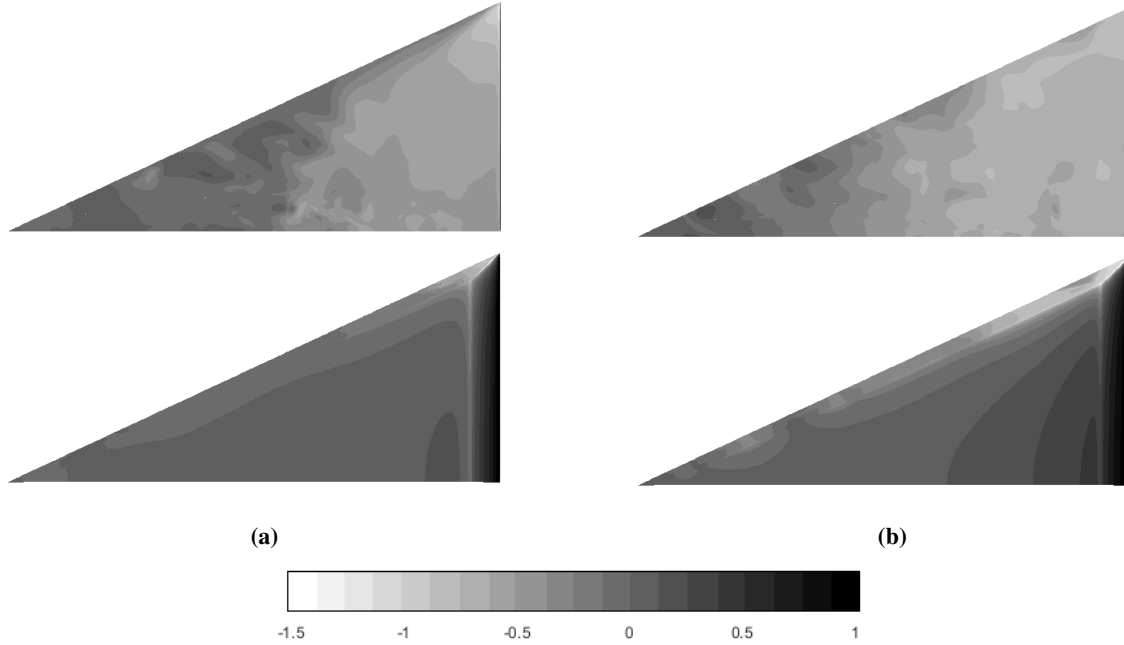
13

Fig. 8   Instantaneous contour maps, at non-dimensional time $t = 150.52$**, of the pressure coefficient** C_p **on the leeward (top row) and windward (bottom row) surfaces of a RDW at angles of attack** $\alpha = 10°$ **(column (a)) and** $\alpha = 20°$ **(column (b)) and** $Re_\infty = 3.4 \times 10^5$**.**

confining the spanwise vortices, which induces substantial suction, to the leeward side of a RDW. Therefore, the apparent cooperation between tip and spanwise vortices enhances the lift performance of a RDW.

Figure 8 shows the instantaneous contour maps, at non-dimensional time $t = 150.52$, of the pressure coefficient C_p over the upper and lower (leeward top row and windward bottom row) sides of a RDW at angles of attack $\alpha = 10°$ (column (a)) and $20°$ (column (b)) and $Re_\infty = 3.4 \times 10^5$. The instantaneous C_p distribution over the leeward surfaces shows, in both cases, the presence of a region of low-pressure (suction) that starts at the leading edge of the RDW and covers a large portion of the wing upper surface area. Note the pressure is minimal at the corner at the end of the leading edge where the effect of the downwash induced by the tip vortex is felt the most. With increasing angle of attack from $10°$ (column (a)) to $20°$ (column (b)), the area of the suction region increases and extends further downstream and, therefore, the magnitude of the lift force increases. Note that the pressure distribution over the leeward side of the wing is not uniform and the visible patchiness is the footprint of the spanwise vortices that are convected downstream while pairing and reorganizing. On the other hand, the pressure distribution on the windward side is mostly steady. At both angles of attack, the color maps indicate that the pressure distribution is subdivided in three main regions because the windward side is $15°$ beveled at the edges. Moving along the chord of the RDW from the leading edge to the back apex, the pressure decreases slowly from the maximum at the leading edge to ambient pressure at the apex.
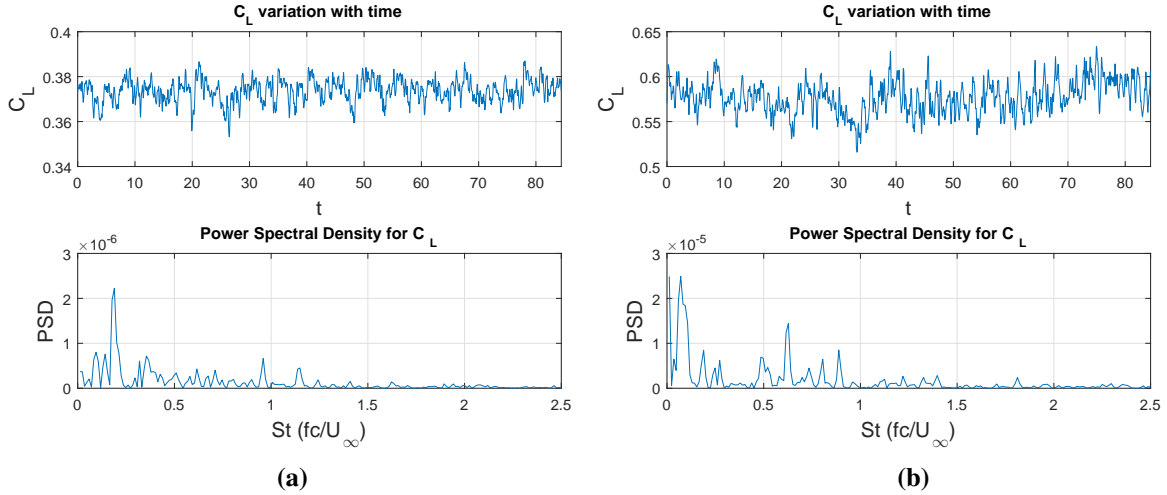
Fig. 9 **Time histories and PSD's of the lift coefficients generated by a RDW at angles of attack** $10°$ **(a) and** $20°$ **(b) and** $Re_\infty = 3.4 \times 10^5$**.**

B. Power spectral density analysis

Figure 9 presents the time histories of the lift coefficients (top row) generated by a RDW at angles of attack $\alpha = 10°$ (panel(a)) and $20°$ (panel(b)) and the associated PSDs (bottom row). For both angles of attack, the magnitude of oscillations of the lift coefficients are not negligible and amount to about 9% when $\alpha = 10°$ (panel(a)) and 19% when $\alpha = 20°$ (panel(b)). To understand the nature of such an unsteady time evolution, we perform a PSD analysis. In both cases, the PSDs show a dominant peak at a well-defined Strouhal number ($St = fc/U_\infty$, where f is the frequency of oscillation), which decreases as the angle of attack increases: $St = 0.19$ at $\alpha = 10°$ (panel (a)) and $St = 0.07$ at $\alpha = 20°$ (panel (b)). The PSDs in figure 9 also show that at both angles of attack, the largest peak is surrounded by several lower peaks, especially at higher Strouhal numbers. Figure 6 suggests that the higher peaks in the PSDs plots identify phenomena such as vortex shedding, pairing and reconfiguration. However, figure 6 does not provide sufficient insight to determine to which phenomenon each peak is related.

Note that the PSD analysis of the time evolution of the drag coefficient (not shown) identifies identical frequencies as the ones shown in figure 9 bottom row. This can be explained by considering the total drag as the sum of the zero-lift drag plus the lift-dependent drag plus the compressibility drag. In our case the first and third term are negligible with respect to the lift-dependent drag or induced drag. Note that the induced drag term is more than just the inviscid drag induced by wake. This term can be expressed as the sum of a viscous and inviscid contributions. In our case, the inviscid contribution is due to the lift-dependent drag that depends on the geometry of the planform, while the viscous contribution is due to the increase of skin friction and pressure drag with changes in angle of attack. Such increases are generated by the increased velocities on the leeward side of the RDW leading to higher shear stresses and more severe adverse pressure gradients with corresponding increase in pressure drag. Consequently, it is not surprising that the

PSDs of the lift and drag coefficients are, up to a scaling factor, nearly identical.

In order to understand which phenomena are identified by the higher peaks of the PSD plots (see figure 9), we analyze a sequence of two instantaneous snapshots of the pressure and vorticity fields past a RDW at angles of attack $\alpha = 10°$ (panels (a) and (c)) and $\alpha = 20°$ (panels (b) and (d) of figure 10). Each panel comprises of three subfigures: the top subfigure show the distribution of the pressure coefficient C_p, the middle one presents the distribution of the y-component of the vorticity field ζ_y, both shown at the symmetry plane and the bottom subfigure shows the chordwise distribution of the pressure coefficient over the leeward (black line) and windward (gray line) sides of the RDW.

The structure of the vorticity field is shown by the center subfigure of each panel of figure 10. At both angles of attack, the sequences of snapshots show that the shear layer that separates from the leading edge of the RDW rolls-up forming vortices of negative y-vorticity component. These vortices are shed into the flow over the leeward side of the RDW, and convected downstream where they sometimes pair together while their strengths decrease due to viscous dissipation. The dye visualization shown in figure 1 (b) further validates the accuracy of our simulations, as the comparison with the center subfigure of figures 10 (b) and (d) shows.

The top subfigure in each panel of figure 10 shows the distribution of the pressure coefficient, C_p. The effect of the vorticity distribution, discussed above, is to create a large suction bubble, of light gray color, located above the front half of the leeward side of the RDW, a bubble whose size increases with increasing angle of attack. To complement this low pressure bubble, there is high pressure bubble, of dark gray color, on the front of the windward side of the RDW. The combined beneficial lift effects of these two pressure bubbles is reflected by the chordwise pressure distribution shown in the bottom subfigure of each panel.

Each panel of figure 10 can be easily analyzed and interpreted by tracing vertical lines that cross all three subfigures. This approach reveals the close relationship between vortices, in particular vortex cores, shown in the middle subfigure, and spots of minimal pressure, represented by the white circular blobs in the top subfigure. In the bottom subfigure the black line identifies the pressure values induced on the leeward side by the vortices moving above. It allows to better understand the pressure footprint, shown in the top row of figure 8, generated by the vortical structures shown in figure 6.

The time evolution of the vortical flow and consequent evolution of the pressure field can be analyzed by tracing vertical lines that span both panels (a) and (c) for $\alpha = 10°$ and (b) and (d) for $\alpha = 20°$. For example, select a white blob on panel (a) and draw a line through the blob that spans both panels (a) and (c). Identify the same white blob on panel (c) and draw a line through the blob that spans both panels (a) and (c). The time lapse between the first line and second line is 10 time steps. Using the two lines as a reference, we can gain insight on the time evolution of the flow over a RDW. In particular, this exercise shows how quickly certain features change with time.

We can now explain the relationship between the structure of the vorticity field (center subfigure in all panels) and the complex unsteady pressure distribution over the leeward side of the RDW shown by the black line in bottom subfigure in all panels. We start discussing the simpler case where the RDW is at an angle of attack of $\alpha = 20°$ (see
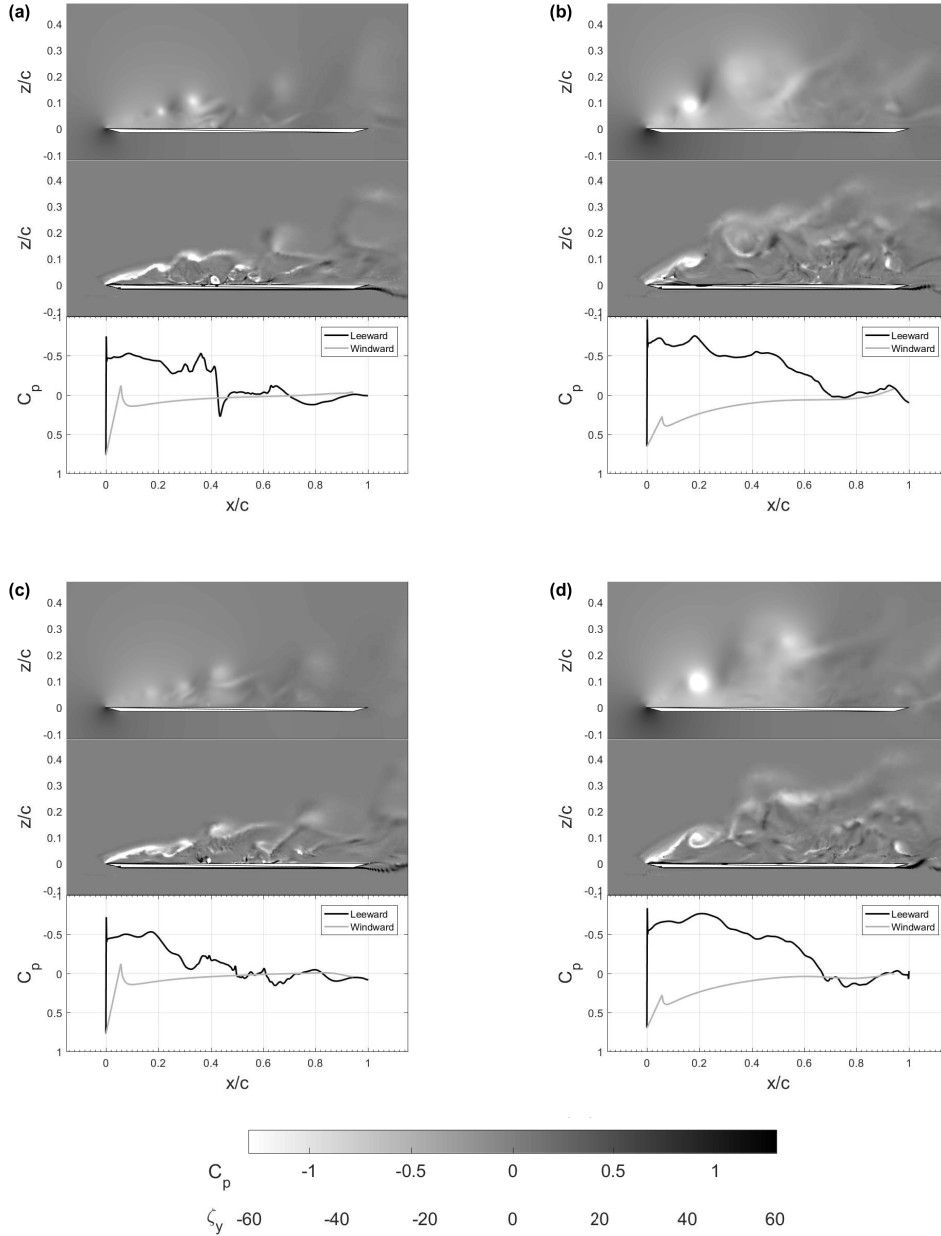
Fig. 10   Sequence of instantaneous snapshots showing the contour maps of the pressure coefficient and the y-component of vorticity at the symmetry plane with the associated pressure coefficient distribution over the leeward and windward sides of a RDW at time instants 150.92 and 151.12 , and at angles of attack $\alpha = 10°$ ((a) and (c)) and $\alpha = 20°$ ((b) and (d)).

figure 10 (b)-(d)). In this case, the evolution of the shear layer takes place well above the leeward side of the RDW minimizing, therefore, the interaction between the roll up of the shear layer and the boundary layer present on the surface of the RDW is minimal. The pressure distribution on the leeward side (bottom subfigure of the panels) is not monotonic, the maxima of suction represent the footprints of the vortices generated by the roll-up of the shear layer (see

center subfigure of the panels). For example, in panel (b) the bottom subfigure shows a peak of suction located at about $x/c = 0.18$, where is located the core of a forming vortex and associated blob of minimum pressure. Panel (d) shows how quickly the distributions can change. After 10 time steps, the vortex and associate pressure blob have grown larger and the peak of suction on the leeward side has substantially broadened. Therefore, as time lapses, new vortices are created and, correspondingly, new peaks appear in the pressure distribution, while previous peaks move downstream decreasing in amplitude as the associated vortices are convected downstream losing strength. It is, therefore, clear that the contribution to lift due to the suction acting on the leeward side of the RDW is due to the combined action of the vortices generated by the roll-up on the shear layer. This fact explains the oscillations observed in the time evolution of the lift coefficient shown in figure 9 (b).

We can now discuss the complex relationship between the structure of the vorticity field and the pressure distribution on the leeward side of the RDW at angle of attack $\alpha = 10°$, see figure 10 (a) and (c). Contrary to the previous case where $\alpha = 20°$, the pressure distribution in this case presents minima of positive pressure, sometimes broad, sometimes spiky. Such a complex pressure distribution is a consequence of the strong interaction between the roll up of the separating shear layer and the boundary layer over the leeward side of the RDW. Because of the low angle of attack, the roll-up takes place close to the upper surface of the RDW, and the shed vortices interact with the boundary layer generating secondary vortices over the leeward side of the RDW. For example, in panel (a), surprisingly, a spike of high pressure is located at about $x/c = 0.44$. Using the lines technique described above, one can see that the sudden increase in pressure is due to a vortex that at this instant lies near the leeward side of the RDW. The vortex core at $x/c = 0.41$ corresponds to a small peak of suction then, moving to the right, the pressure increases suddenly as the flow induced by the vortex becomes perpendicular to the leeward side. As in the previous case, after 10 time steps, the vortex is replaced by a pair of small vortices of opposite signs and the sharp spike in pressure is replaced by a lower and broader pressure increase. Even more complex and unpredictable is the pressure distribution over the back two thirds of the leeward side of the RDW due to the complex and unpredictable interactions of the shed vortices with the boundary layer. On the other hand, it is interesting to notice that the pressure distribution over the front third of the RDW is often smooth and almost constant, because the shear layer at angle of attack $\alpha = 10°$ rolls up further downstream than in the case $\alpha = 20°$, and the smooth vortex sheet induces an almost constant suction, as clearly shown by panels (a) and (b) of figure 6.

We are now ready to interpret the results presented by the PSDs shown in figure 9. Based on the snapshots in figure 10, that show the vorticity and pressure fields on the symmetry plane, it is tempting to identify the higher peaks of the PSDs in figure 9 as the frequency of shedding of the spanwise vortices. However, for both angles of attack $\alpha = 10°$ and $\alpha = 20°$, an estimate of the frequencies of shedding based on sequences of snapshots (not shown here) longer than in 10 appears to indicate that the frequencies of shedding are higher than the frequencies of the higher peaks of the PSDs shown in figure 9.

To identify correctly the frequencies of shedding, we place a virtual probe able to measure the magnitude of the

18

y-component of the vorticity field at $x/c = 0.3$ and $z/c = 0.08$ when $\alpha = 10°$ and $x/c = 0.3$ and $z/c = 0.2$ when $\alpha = 20°$. As can be seen in figure 10, the locations chosen for the virtual probe are on the path of vortices shed from the leading edge. Figure 11 shows the time histories of the y-component of the vorticity (top row) and the associated PSDs (bottom row) for the flow past a RDW at angles of attack $\alpha = 10°$ (panel(a)) and $\alpha = 20°$ (panel (b)).
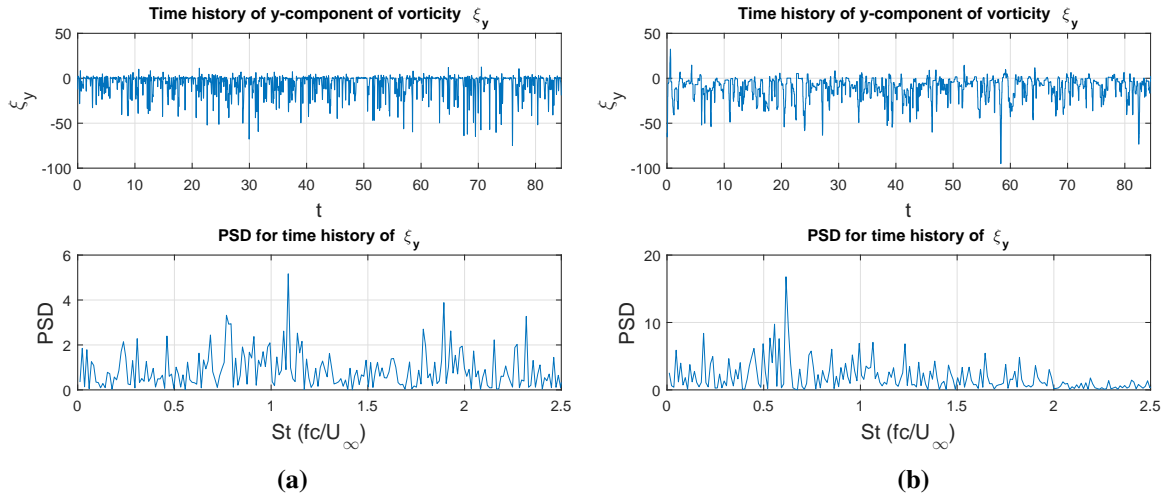

Fig. 11 Time histories and PSDs of the y-component of the non-dimensional vorticity field ξ_y obtained by placing a probe in the flow past a RDW at angles of attack $10°$ (a) and $20°$ (b) and $Re_\infty = 3.4 \times 10^5$.

To understand the relationship between the PSDs of the lift coefficients and the PSDs of the y-component of the vorticity fields in the symmetry plane, it is important to remember that the time evolution of the lift coefficient (figure 9, top row) is related to the lift generated by the entire RDW and, therefore, reflects the unsteady the contribution to lift due to the three-dimensional vorticity fields shown in figure 6. On the other hand, the information depicted in figure 11 is restricted to the symmetry plane.

Panel (a) of figure 11 shows the time evolution of the y-component of the vorticity field (top) and the associated PSD for the angle of attack $\alpha = 10°$. The y-component of the vorticity field shows oscillations whose frequency and amplitude changes with time, indicating that the shedding process is not synchronous, due to the strong interaction between the shear layer roll up and the boundary layer, as the snapshots in figure 10 corroborate. Nevertheless, the PSD presents a dominant peak at $St = 1.09$, which is the main frequency of shedding. The PSD shows also some important secondary peaks probably due to the asynchrnous nature of the vortex shedding process. We believe that this peak correspond to the peak of the PSD of the lift coefficient located at 1.15, see bottom subfigure of panel (a) of figure 9. Similarly, panel (b) of figure 11 shows the time evolution of the y-component of the vorticity field (top) and the associated PSD for the angle of attack $\alpha = 20°$. Note how in this case the frequency and amplitude of oscillation are substantially lower than in the case $\alpha = 10°$. Furthermore, the oscillations are not as asynchronous as in the previous case. It is not surprising, therefore, that the frequency of vortex shedding is clearly identified by a single peak

at $St = 0.61$. Note that the secondary vortices are smaller than in the previous case, corroborating the fact that the shedding mechanism is less asynchronous than $\alpha = 10°$. This peak clearly corresponds to the peak of the PSD of the lift coefficient located also at $St = 0.61$, see bottom subfigure of panel (b) of figure 9.

We can now discuss the physical mechanisms responsible for the dominant peaks located at $St = 0.19$ when $\alpha = 10°$ and $St = 0.07$ when $\alpha = 20°$ in the PSDs of the time evolution of the lift coefficients, see bottom subfigures of panels (a) and (b) of figure 9, respectively. The instantaneous iso-surfaces of the vorticity fields shown in figure 6 depict the complex three-dimensional structure of the vorticity field. Such unsteady structures are produced by the pairing, realignment and reorganization of the spanwise vortices generated by the roll-up of the shear layer separating from the leading edge of the RDW. Obviously, pairing and reorganization of the spanwise vortices has to happen on time scales slower than the time scales of vortex shedding identified above. Therefore, we can conclude that the dominant peaks of the PSDs shown in panels (a) and (b) of figure 9 identify the frequencies of three-dimensional reorganization of the vortical structures convected over the leeward side of the RDW. These are the structures that contribute the most to the generation of lift and are also responsible for the unsteadiness of lift.

C. Comparisons with experimental data

In this section, we present our numerical estimates of the aerodynamic forces acting on a DW and a RDW and compare them with some experimental results available in literature, which have been obtained under similar flow conditions. In figure 12, we present the lift and drag coefficients of a DW to validate our numerical approach, and in figure 13 we present our estimates of the aerodynamic forces acting on a RDW.

Figure 12 compares numerical and experimental estimates of lift, C_L (panel (a)), and drag, C_D (panel(b)), coefficients for a DW over a wide range of angles of attack . The comparison is made between our study and the experimental studies presented by Guy *et al.* (2000) [25] (65° sweep, $Re = 4.9 \times 10^5$), Li and Wang (2003) [26] (40° sweep, $Re = 2.5 \times 10^5$), Zhan and Wang (2004) [27] (70° sweep, $Re = 3.16 \times 10^5$), Altaf *et al.* (2011) [5] (75° sweep, $Re = 3.82 \times 10^5$), Ludin Jamaluddin *et al.* (2015) [16] (75° sweep, $Re = 3.82 \times 10^5$) and Ko (2016) [7] (65° sweep, $Re = 3.45 \times 10^5$), which considered flows past a DW at Reynolds numbers close to the one considered in this study.

Figure 12(a) shows that the lift coefficients for a DW reported by the studies we use as a comparison and validation where the sweep angles of the wing planforms range from 40° to 75° and the Reynolds numbers range from 2.5×10^5 to $4,9 \times 10^5$. Our estimates for C_L (black solid squares) match accurately the experimental results by Ko [7] (2016) (gray solid circles), where the wing planform (65° sweep angle) and the Reynolds number (3.4×10^5) are exactly the same. Our results are also in very good agreement with those by Guy *et al.* [25] (2000) (long-dashed line), who used a DW with 65° sweep angle at $Re_\infty = 4.9 \times 10^5$. Understandably, we observe a lesser agreement with the results by Li and Wang [26] (2003) (short-dashed line) and Altaf *et al.* [5] (2011) (gray solid triangles) probably because of the larger differences in the wing sweep angles and Reynolds numbers used. An even far lesser agreement is with the numerical
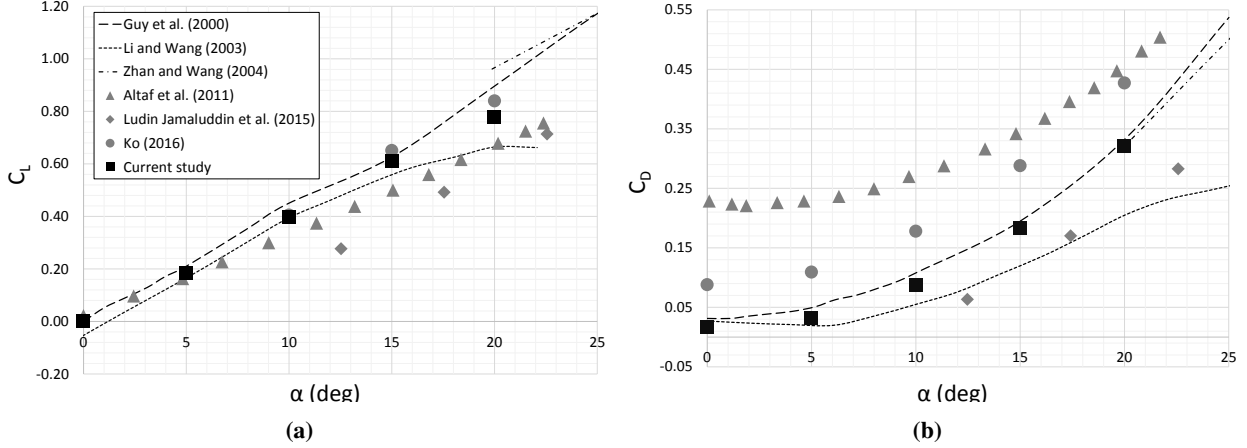
Fig. 12 Comparison between numerical and experimental estimates of the lift coefficient, C_L (a), and drag coefficient, C_D (b), of a DW over a wide range of angles of attack

results by Ludin Jamaluddin *et al.* [16] (2015), where the data obtained through steady state simulations seem to be affected by some setting error. In fact, by linearly extrapolating the data, $C_L = 0$ corresponds to an angle of attack of about $5°$.

Figure 12(b) compares numerical and experimental estimates of the drag coefficient, C_D, of a DW. It shows that our numerical estimates match accurately the experimental results by Guy *et al.* [25] (2000), although in the experiment the sweep angle is $70°$ and $Re_\infty = 4.9 \times 10^5$. Further validation of our results is provided, at angle of attack of $20°$, by Zhan and Wang [27] (2004), who used a DW with $70°$ sweep angle at $Re_\infty = 3.16 \times 10^5$. The agreement with the results by Li and Wang [26] (2003) is accurate only at angle of attack $\alpha = 0°$, where C_D is due to skin-friction only, because of the substantial difference in the planform sweep angle, which, in the experiment, is of only $40°$. Surprisingly, the agreement with the results by Ko [7], that used our same wing planform and Reynolds number, is not accurate. At all angles of attack, the trend is the same as our and Guy *et al.* [25] trends, but the values of C_D are higher, by almost a constant amount of about 0.07. Even worse is the comparison with the data by Altaf *et al.* [5], where the value of the drag coefficient at zero angle of attack is above 0.2 and the trend is more similar to the trend of data by Li and Wang [26]. At zero angle of attack, the only source of drag should be the skin-friction generated by the boundary layer that develops over the wing. Such a contribution to drag is small, and for thin planforms is of the order of 10^{-2}. From an experimental point of view, the discrepancies at zero angle of attack could be due to an imprecise calibration of the experimental apparatus, or a slight misalignment of the model when mounted on the support, or the data were imprecisely tared during post-processing. From a numerical point of view, further motives for small disagreements could be due: 1) to the roughness of the wing surface, which is finite in the experiment, but zero in the numerical simulations; 2) to the perfectly sharp leading edge that in the experiment cannot be manufactured; 3) to the use of the RANS turbulence model in the boundary layer region, which could be not perfectly accurate. This being said, it is noticeable, that if

we shift down Ko [7] data by a factor of about 0.07, so that their drag coefficient at zero angle of attack matches the value of our, Guy *et al.* [25] and Li and Wang [26] estimates, we obtain an excellent agreement also with Ko [7] data. The numerical results by Ludin Jamaluddin *et al.* [16] (2015) were supposed to replicate the experimental results by Altaf *et al.* [5] (2011) by using the same wing planform and Reynolds number. However, the steady state numerical simulation predicts a substantially lower drag than the experiment. Again, it seems that the steady state simulation is affected by some setting error, since C_D appears to go to zero for about $\alpha = 5°$.

The above detailed comparisons between our numerical results and several experimental investigations successfully validate our numerical approach. As for the lift coefficient, there is excellent agreement between our data and Guy *et al.* [25] and Ko [7] data. As for the drag coefficient, there is an excellent agreement with Guy *et al.* [25] and Li and Wang [26]. We discussed the reasons for the disagreement with Ko [7] results and argued how to reconcile the two sets of data. Based on this successful validation, we move ahead to discuss our results for a RDW. Note that the simulations for a RDW are performed by simply rotating by 180° the computational domain and, therefore, the results for a RDW are as reliable as those, just discussed, for a DW. This simple rotation of the wing mimics the experimental set up by Ko [7], where the wing model was mounted rotated by 180° on the force balance.

Figure 13 compares our numerical estimates of the coefficients of lift, C_L panel (a), and drag, C_D panel(b), of a RDW with all, to the best of our knowledge, experimental results available in literature, i.e., the studies by Ko [7] (2016) and Altaf *et al.* [5] (2011). We are also comparing our results with the only numerical study available, the one by Ludin Jamaluddin *et al.* [16] (2015), that reported results only for angles of attack $\alpha > 25°$.
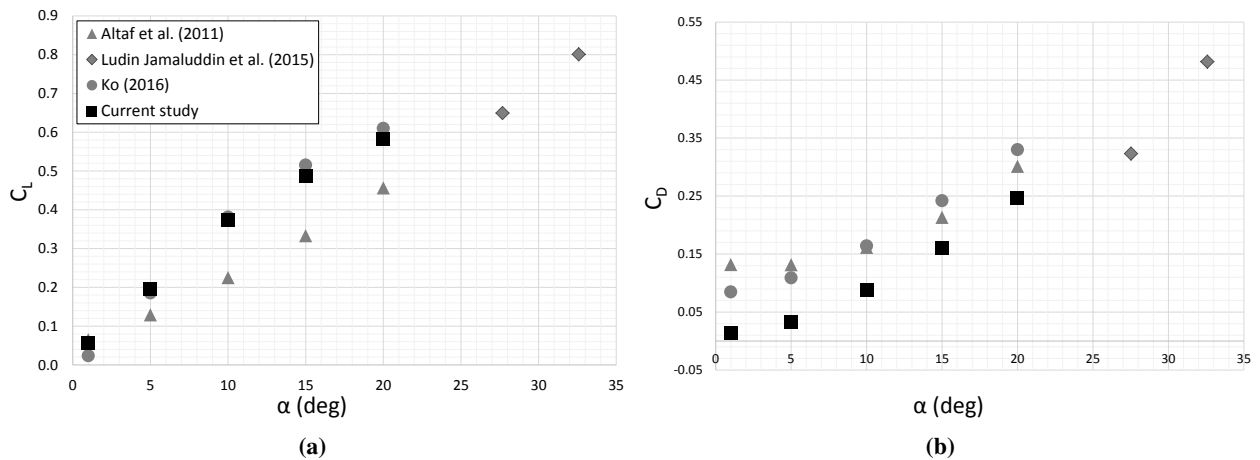

Fig. 13 **Comparison between numerical and experimental estimates of the lift coefficient, C_L (a), and drag coefficient, C_D (b), of a RDW over a wide range of angles of attack**

Figure 13 (a) shows that our numerical estimates (black solid squares) for the lift coefficient, C_L, of a RDW are, overall, in excellent agreement with the experimental results by Ko [7] (2016) (gray solid circles) obtained using the same wing planform (65° sweep angle) and the Reynolds number (3.4×10^5) as us. The largest discrepancy is at angle

22

of attack $\alpha = 1°$, where we predict a C_L twice as higher as in the experiment by Ko [7] (2016), probably because in the our simulation the leading edge of the RDW is perfectly sharp and exactly beveled by 15°, therefore generating a small lift even at very small angles of attacks. Note that we could not simulate the case at angle of attack $\alpha = 0°$ because the simulation was not converging, probably because of the singular line represented by the perfectly sharp leading edge. At angles of attack $\alpha = 10°$ and $\alpha = 15°$ the agreement is excellent. The agreements deteriorates minimally at angles of attack $\alpha = 15°$ and $\alpha = 20°$, where our numerical simulation underestimates by a bit C_L. This discrepancy is probably due to the fact that our simulation is symmetric with respect to the mid-chord of the RDW and, therefore, underestimates the effects of the asymmetric three-dimensional vortical flow that in reality develops over the RDW. The discrepancy with the results by Altaf *et al.* [5] (2011) is much larger than in the DW case, probably because of the differences in the geometry of the wing planforms and the greater complexity of the unsteady flow. A direct comparison with the results by Ludin Jamaluddin *et al.* [16] (2015) is impossible, because their range of angles of attack is beyond the range covered in our study. However, they seem to complement nicely the results by Altaf *et al.* [5].

Figure 13 (b) shows the values of the drag coefficient, C_D, estimated numerically and measured experimentally for a RDW. Not surprisingly, the data reported in 13 (b), show the same discrepancies as in 12 (b) for a DW. As in the case of a DW, Ko [7] data are, at zero angle attack, higher by a factor of about 0.07 and the data for all angles of attack are shifted higher by about the same amount. Since our and Ko [7] data have the same trend, it is easy to envision that if Ko [7] data are lowered by a factor of about 0.07, there will be an excellent agreement between the two sets of data. The same cannot be said comparing our and Altaf *et al.* [5] results because the error at zero angle of attack is different from the same error for the DW and also the trend is not the same. In other words, it appears impossible to reconcile Altaf *et al.* [5] results with the other sets of data. Finally, the steady state numerical predictions of the drag coefficient by Ludin Jamaluddin *et al.* [16] seem to be at odds with all other sets of data, by substantially underpredicting C_D.

D. Aerodynamic performance of DW versus RDW

Figure 14 compares the numerically estimated coefficients of the aerodynamic forces generated by a DW and an identical RDW at angles of attack $\alpha = 1°$, 5°, 10°, 15° and 20°: lift, C_L panel (a), drag, C_D panel (b) and the lift-to-drag ratio, C_L/C_D panel (c). At low angles of attack ($\alpha = 1°$, 5° and 10°), both wings generate nearly the same lift (panel (a)) and drag (panel (b)). At higher angles of attack ($\alpha = 15°$ and 20°), however, the DW generates higher lift but also induces higher drag than the RDW. Interestingly, the lift-to-drag ratio of both wings, panel (c), is almost the same: at angle of attack $\alpha = 15°$, for the DW we have $C_L/C_D = 3.30$ while for the RDW it is 3.06; at angle of attack $\alpha = 20°$, for the DW we have $C_L/C_D = 2.41$ while for the RDW it is 2.37. Only at angle of attack $\alpha = 1°$, the lift-to-drag ratio of the RDW is almost twice as high as that of DW, because at this angle of attack the beveled leading edge of the RDW generates a small amount of lift, but higher than that produced by the DW.

Figure 15 compares the quarter-chord pitching moment coefficients $C_{m,c/4}$ of a DW and a RDW. This coefficient
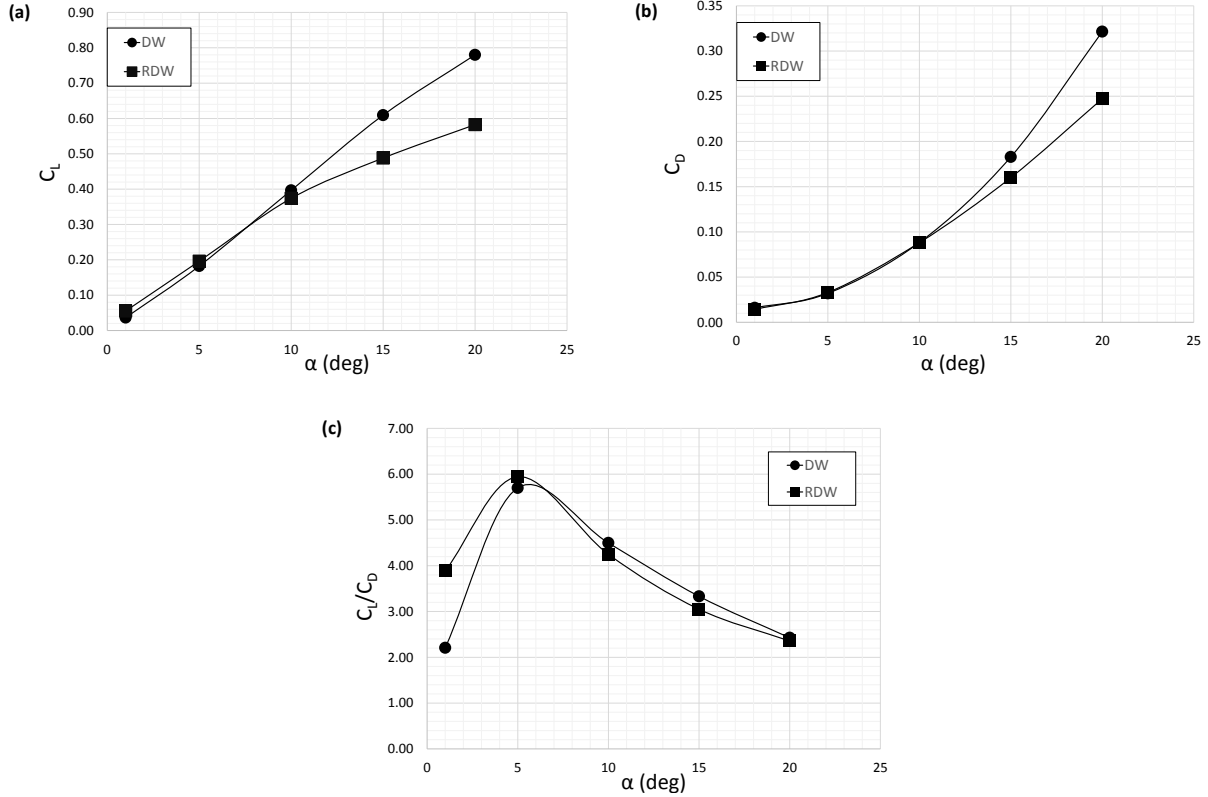
Fig. 14 Comparison between the aerodynamic forces induced by a DW and a RDW at $Re_\infty = 3.4 \times 10^5$**: lift coefficient** C_L **(a), drag coefficient** C_D **(b) and lift-to-drag ratio** C_L/C_D **(c)**

is defined as $C_{m,c/4} = M_{c/4}/(q_\infty Sc)$, where $M_{c/4}$ is the quarter-chord pitching moment. Surprisingly, the RDW produces an almost constant ($0.05 \leq C_{m,c/4} \leq 0.08$) stabilizing moment coefficient, while the DW generates a destabilizing moment whose magnitude decreases almost linearly with angle of attack from $C_{m,c/4} = -0.05$ at $\alpha = 5°$ to $C_{m,c/4} = -0.22$ at $\alpha = 20°$. The pitching moment coefficient of a RDW being almost constant indicates that the aerodynamic center is located close to quarter-chord location.
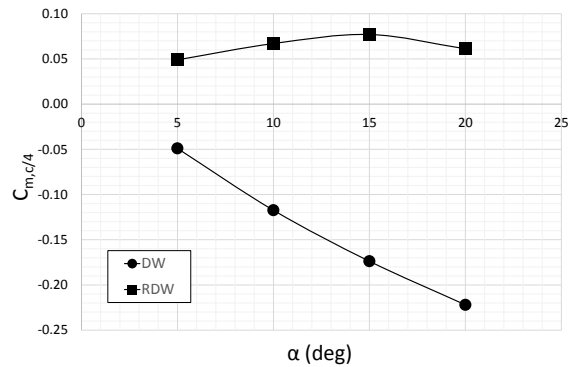

Fig. 15 Comparison between pitching moment coefficient $C_{m,c/4}$ **of a DW and a RDW**

24

The analysis of chordwise pressure coefficient distributions, shown in the bottom subfigure of each panel of figure 10, allows us to explain why the quarter-chord pitching moment coefficient of a RDW is almost constant and weakly stabilizing. In general, the pressure coefficient distribution of a RDW is substantially different from that of conventional wing at the same angle of attack, in the former case, in fact, the peak suction is located at a further upstream chordwise location and the adverse pressure gradient is milder. In particular, the center of pressure at the middle plane of a RDW is located at $x/c = 0.13$ for $\alpha = 10°$ and at $x/c = 0.24$ for $\alpha = 20°$, both upstream of the quarter-chord ($x/c = 0.25$) explaining why the quarter-chord pitching moment has a stabilizing effect. Furthermore, as the angle of attack increases, lift also increases but the moment arm decreases, compensating for the variation in lift and, therefore, maintaining the pitching moment almost constant. Differently, in the case of a DW, the chordwise pressure coefficient distribution is almost constant when compared to a RDW, while the suction peaks are located underneath the cores of the leading edge vortices. Thus, the location of the center of pressure of a DW is constant and located downstream the quarter-chord $x/c = 0.25$. Therefore, as the angle of attack increases, lift increases and, consequently, the pitching moment becomes more negative.

It is the almost constant stabilizing pitching moment that makes the RDW an excellent candidate for designing WIG-crafts. In the design of a WIG-craft, the flat planform presented in this conceptual study is modified to address aerodynamic, structural and practical requirements. In a WIG-craft, each cross section of the RDW has airfoil profile instead of being flat, therefore modifying the shear layer separation at the leading edge. In correspondence of the centerline of the RDW, where the vortical structures reorganize themselves generating undesirable lift fluctuations, the WIG-craft has the fuselage that modifies substantially the unsteady effect of the vortical flow. Finally, the tips of the RDW of a WIG-craft are modified by the addition of aerodynamic floating devices and winglets that modify substantially the tip vortices. Therefore, in the design of a WIG-craft there is the opportunity of taking advantage of the almost constant stabilizing pitching moment of a RDW, while suppressing the undesirable unsteadiness present in the aerodynamic forces.

V. Conclusions

We numerically simulated and analyzed the structure and time evolution of the vortical flow over a RDW, in order to understand and quantify its impact on the aerodynamic performance of such a wing. As a validation, we simulate the flow past the same planform and Reynolds number as in the experiments by Ko [7] and Lee and Ko [8], and our results complement and extend their experimental findings. First of all, we established that, contrary to the flow over a DW, the flow past a RDW is always unsteady, even at small angles of attack and, therefore, only an unsteady simulation can reproduce such a flow accurately.

Using flow visualizations, we established, in agreement with experimental findings, that two are the main features of the vortical flow that develops over a RDW: the spanwise vortical structures and the tip vortices. The shear layer

separating from the leading edge creates the spanwise vortical structures, which pair, realign and reorganize themselves as they are convected downstream, creating a complex narrow wake. The spanwise vortical structures are responsible for a substantial portion of the lift generated by a RDW. The shear layers separating from the side-edges roll up away from the wing planform forming the tip vortices. The velocity vector field shows that the downwash induced by a tip vortex impact on a limited area of the wing, contributing weakly to the production of lift. Surprisingly, the formation of the tip vortices and spanwise vortices seem to be nearly independent of each others. Nevertheless, the tip vortices, which directly contribute little to the production of lift, contribute indirectly to its production by confining the spanwise vortices to the leeward side of the RDW.

We established a clear relationship between the vorticity and pressure fields. In particular, we showed that the minima of the pressure field identify accurately the cores of the spanwise vortices. The time evolution of the spanwise vortices generates an unsteady pressure distribution over the leeward side of the wing, which is responsible for the non-negligible oscillations affecting both drag and lift coefficients. At the contrary, the pressure distribution on the windward side remains steady over most of the wing. PSD analyses of the aerodynamic coefficients show a dominant peak at low Strouhal numbers and a few secondary peaks at higher Strouhal numbers. We established that the frequency of shedding of the spanwise vortices corresponds to one of the secondary peaks. Substantiated by our flow visualizations, we concluded that the paring, realignment and reorganization of the spanwise vortices, which evolve on time scales slower than the frequency of shedding, correspond to the dominant peak present in the PSD and, therefore, are responsible for the oscillations affecting the aerodynamic coefficients.

Our estimates of the aerodynamic forces generated by a RDW agree with and extend the experimental results by Ko [7] and Lee and Ko [8]. The comparison for the aerodynamic performance of a DW versus a RDW is of particular interest. Up to an angle of attack of about $10°$ lift and drag coefficients are nearly the same, while at higher angles of attack, up to $20°$, the DW produces higher lift but also induces higher drag than a RDW. Surprisingly, the lift-to-drag ratio is about the same for both wings. The pitching moment coefficient $C_{m,c/4}$ experienced by a RDW is stabilizing and almost constant up to $20°$, while the pitching moment of a DW is destabilizing and increases almost linearly up to $20°$. In conclusion, the performance of a DW and a RDW are comparable, however, they find applications in very different flow conditions. The RDW could find applications at low-speed near-ground flight conditions, because of its characteristic stabilizing pitching moment. To this end, future work will focus on simulating fully three-dimensional flows past a RDW in near-ground flight conditions.

Acknowledgements

References

[1] Lippisch, A. M., "Ground effects utilizing and transition aircraft," United States Patent No. US3190582A, 1965.

[2] Lippisch, A. M., "Wing arrangement," United States Patent No. US3627235A, 1969.

[3] Heinz A. Gerhardt, "Supersonic Natural Laminar Flow Wing," United States Patent No. US005538201A, 1996.

[4] Urquhart, S., Prince, S., and Khodagolian, V., "Aerodynamic study of reversed-delta wing surface craft in ground effect," *44th AIAA Aerospace Sciences Meeting and Exhibit*, Vol. 5, American Institute of Aeronautics and Astronautics, Reston, Virigina, 9-12 January 2006, pp. 3067–3081. doi:10.2514/6.2006-253.

[5] Altaf, A., Omar, A. A., Asrar, W., and Ludin Jamaluddin, H. B., "Study of the Reverse Delta Wing," *Journal of Aircraft*, Vol. 48, No. 1, 2011, pp. 277–286. doi:10.2514/1.C031101.

[6] Mou, H., "An experimental investigation of the passive control of reverse delta wing vortex flow structure and aerodynamic characteristics," Master's Thesis, McGill University, 2015.

[7] Ko, L. S., "An experimental investigation of the aerodynamics and vortex flowfield of a reverse delta wing," Ph.D. Thesis, McGill University, 2016.

[8] Lee, T., and Ko, L., "Experimental study of the vortex flow and aerodynamic characteristics of a reverse delta wing," *Proceedings of the Institution of Mechanical Engineers, Part G: Journal of Aerospace Engineering*, Vol. 230, No. 6, 2016, pp. 1126–1138. doi:10.1177/0954410015604653.

[9] Lee, T., and He, S. M., "The trailing vortices generated by a reverse delta wing with different wing configurations," *Aerospace Science and Technology*, Vol. 82-83, 2018, pp. 378–393. doi:10.1016/j.ast.2018.08.022.

[10] Lee, T., "Impact of Gurney Flaplike Strips on the Aerodynamic and Vortex Flow Characteristic of a Reverse Delta Wing," *Journal of Fluids Engineering*, Vol. 138, No. 6, 2016, p. 061104. doi:10.1115/1.4032301.

[11] Lee, T., Ko, L., and Tremblay-Dionne, V., "Effect of anhedral on a reverse delta wing," *Proceedings of the Institution of Mechanical Engineers, Part G: Journal of Aerospace Engineering*, Vol. 232, 2018, pp. 2317–2325. doi:10.1177/0954410017715047.

[12] Lee, T., and Su, Y. Y., "Aerodynamic performance of a wing with a deflected tip-mounted reverse half-delta wing," *Experiments in Fluids*, Vol. 53, No. 5, 2012, pp. 1221–1232. doi:10.1007/s00348-012-1352-y.

[13] Altaf, A., Thong, T. B., Omar, A. A., and Asrar, W., "Impace of a Reverse Delta Type Add-on Device on the Flap-tip Vortex of a Wing," *International Journal of Aviation, Aeronautics, and Aerospace*, Vol. 3, No. 3, 2016, p. 012002.

[14] Altaf, A., Thong, T. B., Omar, A. A., and Asrar, W., "Influence of a Reverse Delta-Type Add-On Device on Wake Vortex Alleviation," *AIAA Journal*, Vol. 54, No. 2, 2016, pp. 625–636. doi:10.2514/1.J054436.

[15] Cummings, R. M., Morton, S. A., and McDaniel, D. R., "Experiences in accurately predicting time-dependent flows," *Progress in Aerospace Sciences*, Vol. 44, No. 4, 2008, pp. 241–257. doi:10.1016/j.paerosci.2008.01.001.

[16] Ludin Jamaluddin, H. B., Omar, A. A., and Asrar, W., "Numerical Investiation of the Flow Over Delta Wing and Reverse Delta Wing," *Engineering Applications of Computational Fluid Dynamics, Advanced Structure Materials*, Advanced Structured Materials, Vol. 44, Springer International Publishing, Cham, 2015, pp. 85–101. doi:10.1007/978-3-319-02836-1.

[17] Altaf, A., Private communication, March 2019.

[18] Spalart, P. R., "Detached-Eddy Simulation," *Annual Review of Fluid Mechanics*, Vol. 41, No. 1, 2009, pp. 181–202. doi:10.1146/annurev.fluid.010908.165130.

[19] Menter, F. R., "Two-Equation eddy-visocity turbulence models for engineering applications," *AIAA Journal*, Vol. 32, No. 8, 1994, pp. 1598–1605. doi:10.2514/3.12149.

[20] Menter, F. R., Kuntz, M., and Langtry, R., "Ten Years of Industrial Experience with the SST Turbulence Model," *Turbulence Heat and Mass Transfer 4*, Vol. 4, 2003, pp. 625–632. doi:10.4028/www.scientific.net/AMR.576.60.

[21] Menke, M., Yang, H., and Gursul, I., "Experiments on the unsteady nature of vortex breakdown over delta wings," *Experiments in Fluids*, Vol. 27, No. 3, 1999, pp. 262–272. doi:10.1007/s003480050351.

[22] Robertson, E. D., Chitta, V., Walters, D. K., and Bhushan, S., "On the Vortex Breakdown Phenomenon in High Angle of Attack Flows Over Delta Wing Geometries," *ASME 2014 International Mechanical Engineering Congress and Exposition*, ASME, Montreal, Quebec, Canada, November 2014, pp. 1–9. doi:10.1115/IMECE2014-39354.

[23] Leibovich, S., "The structure of vortex breakdown," *Annual Review of Fluid Mechanics*, Vol. 10, No. 20, 1978, pp. 221–246.

[24] Visbal, M. R., and Reno, I., "Computational and Physical Aspects- of Vortex Breakdown on Delta Wings," *33rd Aerospace Sciences Meeting & Exhibition*, Reno, New Virginia, 1995. doi:10.2514/6.1995-585.

[25] Guy, Y., Morrow, J., and McLaughlin, T., "Experimental study of a delta wing with upper and lower flaps," *18th Applied Aerodynamics Conference*, American Institute of Aeronautics and Astronautics, Reston, Virigina, 14-17 August 2000, pp. 118–126. doi:10.2514/6.2000-4003.

[26] Li, Y. C., and Wang, J. J., "Experimental studies on the drag reduction and lift enhancement of a delta wing," *Journal of Aircraft*, Vol. 40, No. 2, 2003, pp. 277–281. doi:10.2514/2.3120.

[27] Zhan, J.-X., and Wang, J.-J., "Experimental study on gurney flap and apex flap on a delta wing," *Journal of Aircraft*, Vol. 41, No. 6, 2004, pp. 1379 – 1383. doi:10.2514/1.4044.